M. R. Malik and P. Balakumar

Acoustic Receptivity of Mach 4.5 Boundary Layer with Leading-Edge Bluntness

Abstract Boundary layer receptivity to two-dimensional slow and fast acoustic waves is investigated by solving Navier-Stokes equations for Mach 4.5 flow over a flat plate with a finite-thickness leading edge. Higher order spatial and temporal schemes are employed to obtain the solution whereby the flat-plate leading edge region is resolved by providing a sufficiently refined grid. The results show that the instability waves are generated in the leading edge region and that the boundary-layer is much more receptive to slow acoustic waves (by almost a factor of 20) as compared to the fast waves. Hence, this leading-edge receptivity mechanism is expected to be more relevant in the transition process for high Mach number flows where second mode instability is dominant. Computations are performed to investigate the effect of leading-edge thickness and it is found that bluntness tends to stabilize the boundary layer. Furthermore, the relative significance of fast acoustic waves is enhanced in the presence of bluntness. The effect of acoustic wave incidence angle is also studied and it is found that the receptivity of the boundary layer on the 'windward' side (with respect to the acoustic forcing) decreases by more than a factor of 4 when the incidence angle is increased from 0 to 45 deg. However, the receptivity coefficient for the 'leeward' side is found to vary relatively weakly with the incidence angle.

Key Words: Boundary layer, hypersonic, receptivity, stability, transition, bluntness

1 Introduction

Laminar-turbulent transition prediction remains an unsolved problem despite a significant amount of research carried out during the past few decades. The various parameters that influence the location of transition include: leading-edge (or nose) radius, body angle of attack and sweep, surface temperature, surface curvature, pressure gradients and flow chemistry. In addition, parameters such as free-stream vorticity, sound, entropy spots, surface roughness and vibrations all influence the outcome. The first set of parameters primarily determines the nature and level of boundary layer instability. The second set constitutes environmental disturbances that act as 'external' forcing; these disturbances are internalized in the boundary layer through the process of receptivity. Receptivity process assigns the initial amplitude of boundary layer disturbance modes, which then amplify linearly followed by nonlinear saturation and secondary instabilities leading to laminar-turbulent transition.

In order for an unsteady external forcing to excite an instability wave, both the frequency and the wavelength of the forcing disturbance must match with those of boundary-layer instability waves. The spatial scales of free-stream disturbances and boundary-layer instabilities are, in general, significantly disparate. Therefore, a wavelength conversion mechanism is needed for an external disturbance to excite an instability wave in a boundary layer. A strongly nonparallel mean flow, such as the leading-edge flow

---

M. R. Malik and P. Balakumar

NASA Langley Research Center, Hampton, VA 23681

Email: mujeeb.r.malik@nasa.gov

or that in the vicinity of a localized inhomogeneity, has all the required spatial scales for this conversion to take place. It was this realization which formed the basis of Goldstein's [1-2] seminal work on generation of Tollmien-Schlichting waves by long wavelength free-stream disturbances.

In a low-speed boundary-layer, an instability wave induced via the leading-edge receptivity mechanism goes through a region of strong attenuation before amplification in the downstream unstable zone. Therefore, the overall effect of leading-edge receptivity is relatively weak in a low-speed boundary layer compared to, for example, receptivity due to a localized flow inhomogeneity (e.g., curvature discontinuity, wall roughness) located near the neutral point. However, for hypersonic flows, Kendall [3] found flow fluctuations of substantial amplitude within the boundary layer ahead of the locations where instability waves are expected to grow according to linear stability theory. Kendall's measurements were made in a conventional tunnel where the turbulent tunnel wall boundary layers radiate acoustic noise into the test section. In such circumstances, leading-edge receptivity would constitute the dominant source of instability waves in the boundary-layer. It is not clear what will be the source of disturbances in a quiet tunnel or in flight, but high frequency disturbances were detected outside the boundary layer in the F-15 cone flight experiment [4] performed at low supersonic Mach numbers.

There have been a number of investigations conducted on the interaction of acoustic waves with supersonic boundary layers. The interaction of acoustic waves with a supersonic boundary layer using inhomogeneous stability equations was investigated in Ref. [5-6]. One important finding was that due to the interaction, the acoustic waves excite disturbances inside the boundary layer, which are much larger than that in the free stream. The interaction of stream acoustic waves with a non-parallel boundary layer was studied in [7]. The analysis and the calculations showed that the disturbance amplitude inside the boundary layer reach significantly higher values compared to that in the free stream. The study indicated the existence of a critical Reynolds number for optimal excitation of boundary layer disturbances.

For a supersonic boundary-layer with sufficiently high Mach number to allow both first and second Mack modes [8], Fedorov and Khokhlov [9] considered boundary layer response to both the fast (with phase speed C = 1+1/M) and slow (with phase speed C = 1-1/M) acoustic waves. The boundary layer modes excited near the leading edge by the two acoustic waves can be referred to as Mode F and Mode S, respectively, for convenience. The work of Fedorov and Khokhlov [10] and Fedorov [11] identified two receptivity mechanisms in this Mach number regime: (1) leading-edge receptivity and (2) synchronization between Mode F and Mode S. In the latter case, fast acoustic wave excites mode F near the leading edge which transfers its energy to the slow mode as the disturbance propagates downstream in the boundary layer. For an adiabatic wall, Fedorov [11] found that receptivity to slow acoustic waves could be as much as 50 times the receptivity via the fast acoustic waves. Thus, the leading-edge receptivity via the slow mode excitation is much stronger than in the case of inter-modal exchange. Even though Mode F is stable, it could play an important role in some instances in the generation of boundary layer instability process via the inter-modal exchange. According to Fedorov [11], this receptivity mechanism may gain significance in the highly cooled boundary-layers that support second mode instability.

Ma and Zhong [12] performed direct numerical simulation for a Mach 4.5 flat-plate boundary layer to investigate receptivity to fast acoustic waves, i.e. the mechanism of inter-modal exchange. Adiabatic wall boundary condition was used in their study, which employed a fifth-order accurate shock-fitting method. In their work, the plate leading-edge was sharp and the associated singularity was 'ignored' in the numerical simulation. The flow in the leading edge region was computed by using a second-order accurate total variation diminishing (TVD) shock-capturing method. It is not clear how the free stream acoustic disturbances were numerically prescribed in in the region computed by the TVD scheme. In a more recent study, Egorov, Fedrov and Soudakov [13] carried out a similar investigation at a Mach number of 6 whereby simulation of receptivity to slow and fast acoustic waves was performed and the effect of incidence angle was studied. Only the 'sharp' leading-edge case was considered and, therefore, flow in this region was not appropriately resolved.

In this paper we study the receptivity of Mach 4.5 boundary layer including the effect of leading edge bluntness. While this Mach number is in the supersonic regime, it does support Mack's second mode instability which is relevant in hypersonic boundary layer transition. At high Mach numbers, the second mode constitutes the dominant mode of instability with real gas effects only modifying the quantitative results (see Malik [14]). Therefore, Mach 4.5 boundary layer can be considered a model problem for investigation of hypersonic boundary layer receptivity and stability in two-dimensional boundary layers.

In the present study, we employ a fifth-order weighted essentially non-oscillatory (WENO) scheme for spatial discretization and use third-order TVD Runge-Kutta scheme for time integration to solve for the boundary layer receptivity problem. We have selected the flow conditions used by Ma and Zhong [12] except that the flat-plate leading-edge has a finite thickness and the flow around the leading edge is resolved by using a sufficiently dense grid. We assume adiabatic wall condition for steady flow computations. The objectives are to understand the receptivity process near the leading edge of a flat plate whereby the leading edge is properly modeled. Computations are performed to determine whether the slow or the fast acoustic waves are more efficient in generating the instability waves and to estimate the effect of wave incidence angle in generating the instability waves. Computations are also carried out with three different values of leading-edge thickness in order to determine the effect of small bluntness on receptivity and stability of a supersonic boundary layer subject to first and second mode instabilities.

The structure of the rest of the paper is as follows. The governing equations and the numerical solution technique are described in Section 2. Relevant linear stability results and those obtained by solving full Navier-Stokes equations are given in Section3. Final conclusions are drawn in Section 4.

2 Governing Equations and Numerical Method

The partial differential equations solved are the three-dimensional unsteady compressible Navier-Stokes equations in conservation form

$$\frac{\partial}{\partial t} Q_i + \frac{\partial}{\partial x_j} \left(F_{ji} - F_{vji} \right) = 0. \tag{1}$$

$$\text{Here } Q_i = \begin{Bmatrix} \rho \\ \rho E \\ \rho u \\ \rho v \\ \rho w \end{Bmatrix} \quad \left[F_{ji} \right] = \begin{Bmatrix} \rho u_j \\ (\rho E + p) u_j \\ \rho u u_j + \delta_{1j} p \\ \rho v u_j + \delta_{2j} p \\ \rho w u_j + \delta_{3j} p \end{Bmatrix} \quad \left[F_{vij} \right] = \begin{Bmatrix} 0 \\ u\tau_{1j} + v\tau_{2j} + w\tau_{3j} - q_j \\ \tau_{1j} \\ \tau_{2j} \\ \tau_{3j} \end{Bmatrix}. \tag{2}$$

Here (x,y,z) are the Cartesian coordinates, (u ,v ,w) are the velocity components, ρ is the density, and p is the pressure. E is the total energy given by

$$E = e + \frac{u^2 + v^2 + w^2}{2},$$

$$e = c_v T \text{ , } p = \rho R T. \tag{3}$$

Here e is the internal energy and T is the temperature. The shear stress and the heat flux are given by

$$\tau_{ij} = \mu \left\{ \frac{\partial u_i}{\partial x_j} + \frac{\partial u_j}{\partial x_i} - \frac{2}{3} \delta_{ij} \frac{\partial u_k}{\partial x_k} \right\}, \quad q_j = -k \frac{\partial T}{\partial x_j}. \tag{4}$$

The viscosity (μ) is computed using Sutherland's law and the coefficient of conductivity (k) is given in terms of the Prandtl number Pr. The variables ρ, p, T and velocity are non-dimensionalised by their corresponding reference variables ρ_∞, p_∞, T_∞ and $\sqrt{RT_\infty}$ respectively. The reference value for length is computed by $\sqrt{\nu x_0 / U_\infty}$, where x_0 is the location of the beginning of the computational domain from the leading edge in the streamwise direction. For the computation, the equations are transformed from physical coordinate system (x, y, z) to the computational curvilinear coordinate system (ξ, η, ζ) and, hence, the governing equations become

$$\frac{\partial}{\partial t}\overline{Q}_i + \frac{\partial}{\partial x_j}\left(\overline{F}_{ji} - \overline{F}_{vji}\right) = 0. \tag{5}$$

where the components of the flux are related to the flux in the Cartesian domain by

$$\overline{Q}_i = \frac{Q_i}{J}, \quad \left[\overline{F}_{ji}\right] = \frac{J}{|J|}\left[F_{ji}\right] \tag{6}$$

and $J = \left\lceil \dfrac{\partial(\xi,\eta,\zeta)}{\partial(x,y,z)} \right\rceil$.

2.1 Solution Algorithm

A schematic diagram of the computational set up is depicted in Fig. 1. The governing equations are solved using a 5th order accurate WENO scheme for space discretization and using a third order, total variation diminishing (TVD) Runge-Kutta scheme for time integration. These methods are suitable in flows with discontinuities or high gradient regions. These schemes solve the governing equations discretely in a uniform structured computational domain in which flow properties are known point wise at the grid nodes. They approximate the spatial derivatives in a given direction to a higher order at the nodes, using the neighboring nodal values in that direction, and they integrate the resulting equations in time to get the point values as a function of time. Since the spatial derivatives are independent of the coordinate directions, the method can be naturally extended to treat multi-dimensional flow. It is well known that approximating a discontinuous function by a higher order (two or more) polynomial generally introduces oscillatory behavior near the discontinuity, and this oscillation increases with the order of the approximation. The essentially nonoscillatory (ENO) and the improvement of these WENO methods are developed to keep the higher order approximations in the smooth regions and to eliminate or suppress the oscillatory behavior near the discontinuities. They are achieved by systematically adopting or selecting the stencils based on the smoothness of the function, which is being approximated. Description of the WENO and TVD methods is given in Ref. [15], while Ref. [16] considers application to the N-S equations. Details of the solution method employed in the present computation can be found in Ref. [17].

In the present simulation, the blunt flat plate is assumed to align with the free stream. At the outflow boundary, characteristic boundary conditions are used, while at the wall, velocity components are assumed to vanish as is the heat flux. In addition, continuity equation is prescribed at the wall to close the solution. In the mean flow computations, the free-stream values are imposed at the outer boundary, which lies outside the bow shock. In the unsteady computations, acoustic disturbances are superposed on the uniform free stream at the outer boundary. Also, in this case, wall temperature fluctuations are assumed to vanish instead of perturbation heat flux (see [18]).

The computational procedure we adopt is to first compute the steady mean flow by performing unsteady computations using a variable time step (based on a CFL number of 0.3) until the maximum residual reaches a small value ~10^{-11}. After the steady state solution is obtained, the next step is to introduce unsteady disturbances at the outer boundary of the computational domain and to perform time accurate computations to investigate interaction of acoustic waves with the plate leading edge and evolution of instability waves thus generated within the boundary layer. Since we use very fine spatial grid to resolve the leading-edge region, these computations require very small time step which is taken as the minimum time step allowable for a CFL number of 0.3. In the nose region, about 500,000 time steps per cycle are used. The computational domain is divided into two regions and larger time steps can be taken in the downstream region. While the simulation allows nonlinear effects, the forcing amplitude is kept small enough in this study for dominant mechanisms to be governed by linear dynamics.

The acoustic field imposed at the outer boundary is taken to be of the following form:

$$p' = \mathrm{Re}\,al\left\{\tilde{p}e^{i\alpha_{ac}x + i\varepsilon_{ac}y - i\omega t}\right\}. \tag{7}$$

Here α_{ac}, ε_{ac} are the x,y wavenumbers, respectively, of the acoustic wave, and ω is the corresponding frequency. The incident angle θ of the acoustic wave is defined as

$$\theta = \tan^{-1}\frac{\varepsilon_{ac}}{\alpha_{ac}}$$

Here, $\theta = 0$ signifies a wave which is aligned with the free stream while $\theta > 0$ signifies the wave that impinges on the lower side of the plate $y < 0$. Since we are computing the flow field including the leading edge, the unsteady flow field in the upper part of the domain $y > 0$ corresponds to the case $\theta < 0$ and we do not need to perform separate computations for the waves radiating from above and below.

3 Results

Computations are performed for Mach 4.5 flow over a semi-infinite flat plate with a blunt leading edge. The boundary layer at this Mach number is susceptible to both first and second mode disturbances (in Mack's [4] terminology) and, therefore, the associated instability phenomenon is relevant to hypersonic boundary layer transition. Flow conditions are essentially the same as in Ma and Zhong [12]. The difference in the two simulations is that we actually resolve the blunt leading-edge, while they assumed it to be sharp and then essentially overstepped the associated singularity. Table 1 gives the flow parameters and Fig. 1 shows the schematic diagram of the computational set up. The leading edge of the plate is modeled as a super ellipse of the form

$$\frac{(x-a)^4}{a^4} + \frac{y^2}{b^2} = 1. \tag{8}$$

Here b is the half thickness of the plate and computations are performed for several values of thickness $2b$ = 0.0005, 0.005, 0.05 cm. The aspect ratio a/b is taken as 10 hence the blunt leading edge is joined with the straight portion of the plate at $x = 10b$. It should be noted that sharp flat-plate experiments, in general, employ beveled leading edges with very small leading edge radii.

Table 1. Flow parameters used in this study

Freestream Mach number $M_\infty = 4.5$

Free stream Reynolds number $Re_\infty = 7.2*10^6$/m

Free stream density ρ_∞ = 4.319*10^{-2} kg/m^3

Free stream pressure p_∞= 807.57 N/m^2

Free stream velocity U_∞= 728.0 m/s

Free stream temperature T_∞= 65.15 $^\circ$K

Free stream kinematic viscosity ν_∞ = 1.0112*10^{-4} m^2/s

Wall temperature = Adiabatic condition

Prandtl number Pr = 0.72

Ratio of specific heats γ = 1.4

Length scale $\sqrt{\frac{\nu_\infty x_0}{U_\infty}} = 3.727*10^{-4} m.$ ($x_0 = 1.0$ m.)

The boundary layer thickness at x =1 m. δ_0 = 6 mm.

The non-dimensional frequency F is defined as $F = \frac{2\pi\nu_\infty f}{U_\infty^2}$,

where f is the frequency in Hertz. For the above flow conditions, F = 1*10^{-4} corresponds to a frequency of 83.0 kHz.

The grid is generated using analytical formulae. The grid stretches in the η direction close to the wall and is uniform outside the boundary layer. In the ξ direction, the grid is symmetric about the leading edge and is uniform in the flat region. Highly refined grid is employed in the leading-edge region to provide sufficient resolution to capture the receptivity phenomenon in the presence of bluntness. The outer boundary that lays outside of the shock follows a parabola with its vertex located a short distance upstream of the leading edge of the plate. The computational domain extends from x = -0.01 to 2.5 meters in the axial direction. This gives a maximum (square root of length) Reynolds number Re = 4250.0 at the end of the computational domain. Calculations were performed using a grid size of 8001*251. Due to the very fine grid requirement near the nose, the allowable time step is very small and the computations become very expensive to simulate the unsteady computations in the entire domain at once. To overcome this difficulty, calculations are performed in two steps. First, the flow field is computed in the leading-edge region with a very small time step. Second, the flow properties in the middle of this domain are fed as inflow conditions for the second larger domain which allows computations to be performed with a larger time step.

3.1 Linear instability

For future reference, linear stability results for the above flow conditions but using mean flow profiles for compressible Blasius boundary layer are presented in Fig. 2. Figure 2(a) shows the neutral stability diagram in (Re, F) plane for two-dimensional disturbances, both in the first and second mode (see [4]) regimes. Figures 2(b)-(d) show the variation of eigenvalues (α_r, α_i) for the slow (Mode S) and fast (Mode F) modes for the frequencies F = 2.2, 1.1, 0.6 *10^{-4}. The stability curves exhibit the long region of neutrally stable Mack's first mode followed by very narrow strongly unstable second mode region. These modes belong to the slow mode or the Mode S where the phase speed starts from 1-1/M and tends to increase towards the free stream value. On the other hand, the fast mode or the Mode F, for which the phase speed starts from 1+1/M and then decreases, is in general stable (see, however, [10]). At some downstream location the phase speed of mode F equals that of the continuous spectrum with phase speed

C_r = 1.0. These points are marked in the figure and listed in Table 2 for the frequencies F = 2.2, 1.1, 0.6 $*10^{-4}$. At these locations, the decay rate of mode F goes through a jump which is clearly evident for the higher frequency case in Figure 2(b). The synchronization of mode F with Mode S (i.e., where the phase speed of the two discrete modes becomes equal) occurs further downstream well into the second mode unstable region.

Table 2 Locations where phase speed of mode F equals C_r = 1.0 continuous spectra

F	*Re*	*X (m)*
2.2	755	0.079
1.1	1521	0.321
0.6	2804	1.092

3.2 Acoustic waves.

The linearized Euler equations in a uniform mean flow are:

$$
\begin{aligned}
&\frac{\partial \rho}{\partial t} + U_0 \frac{\partial \rho}{\partial x} + \rho_0 \frac{\partial u}{\partial x} + \rho_0 \frac{\partial v}{\partial y} + \rho_0 \frac{\partial w}{\partial z} = 0, \\
&\rho_0 \frac{\partial u}{\partial t} + \rho_0 U_0 \frac{\partial u}{\partial x} = -\frac{\partial p}{\partial x}, \\
&\rho_0 \frac{\partial v}{\partial t} + \rho_0 U_0 \frac{\partial v}{\partial x} = -\frac{\partial p}{\partial y}, \\
&\rho_0 \frac{\partial w}{\partial t} + \rho_0 U_0 \frac{\partial w}{\partial x} = -\frac{\partial p}{\partial z}, \\
&\rho_0 c_p \frac{\partial T}{\partial t} + \rho_0 U_0 c_p \frac{\partial T}{\partial x} = \frac{\partial p}{\partial t} + U_0 \frac{\partial p}{\partial x}, \\
&P_0 = \rho_0 R T_0, \\
&p = \rho_0 R T + \rho R T_0 .
\end{aligned}
\tag{9}
$$

The solution of this system can be written as

$$\begin{Bmatrix} \rho \\ u \\ v \\ w \\ T \end{Bmatrix} = \begin{Bmatrix} \dfrac{1}{a_0^2} \\ -\dfrac{\alpha_{ac}}{\rho_0(\alpha_{ac}U_0 - \omega)} \\ -\dfrac{\varepsilon_{ac}}{\rho_0(\alpha_{ac}U_0 - \omega)} \\ -\dfrac{\beta_{ac}}{\rho_0(\alpha_{ac}U_0 - \omega)} \\ \dfrac{(\gamma-1)T_0}{\rho_0 a_0^2} \end{Bmatrix} p. \tag{10}$$

Here the pressure p is in the form

$$p = p_{amp} e^{i(\alpha_{ac}x + \varepsilon_{ac}y + \beta_{ac}z - \omega t)}. \tag{11}$$

The dispersion relation among the wavenumbers α_{ac}, β_{ac}, ε_{ac} and the frequency ω is given by

$$(\alpha_{ac}U_0 - \omega)^2 = (\alpha_{ac}{}^2 + \beta_{ac}{}^2 + \varepsilon_{ac}{}^2)a_0^2. \tag{12}$$

For acoustic disturbances with zero sweep (i.e., β_{ac}=0), the x-wavenumber α_{ac} can be expressed as

$$\alpha_{ac} = \frac{\omega \cos\theta_y}{(U_0 \cos\theta_y \pm a_0)}. \tag{13}$$

Here $\theta_y = \tan^{-1}\left(\dfrac{\varepsilon_{ac}}{\alpha_{ac}}\right)$ is the incident angle and for $\varepsilon_{ac} < 0$ the plate is radiated from above and for $\varepsilon_{ac} > 0$ the plate is radiated from below or represents the wave which is reflected from the plate. The plus sign corresponds to the fast moving wave and the minus sign corresponds to the slow moving wave. The corresponding phase speeds are $C = U_0 \pm \dfrac{a_0}{\cos\theta_y}$. The wavenumber of the fast moving wave is $\alpha_{ac} < \dfrac{\omega}{U_0 + a_0}$ and for the slow moving wave $\alpha_{ac} > \dfrac{\omega}{U_0 - a_0}$ and the incident angle is limited by $\theta_y < \cos^{-1}\left(\dfrac{1}{M}\right)$. For M = 4.5 and F = 0.6*10^{-4}, wavenumbers of the fast moving and slow moving waves are α_{ac} < 0.1317 and α_{ac} > 0.2070 and the incident angle of the slow moving wave is limited to 77 degrees. Table 3 gives the wavenumbers and the wavelengths in dimensional units for the slow, the fast acoustic waves and the two discrete modes at *Re* = 200.

Table 3 Values of α_{ac} and wavelength for different incidence angles

θ_y	Slow acoustic	Fast acoustic	Slow Stability *Re*= 200	Fast Stability *Re* = 200
0	0.2070 (11.31 mm)	0.1317 (17.77 mm)	0.2024 (11.43 mm)	0.1318 (17.77 mm)
30	0.2166 (10.81 mm)	0.1281 (18.27 mm)	0.2024 (11.43 mm)	0.1318 (17.77 mm)
45	0.2348 (9.97 mm)	0.1225 (19.11 mm)	0.2024 (11.43 mm)	0.1318 (17.77 mm)

The variation of the phase speed with the Reynolds number $Re = \sqrt{U_\infty x / \nu_\infty}$ for two-dimensional slow and fast instability modes are plotted in Fig. 3 for the frequency $F = 0.6*10^{-4}$. The phase speed of the two-dimensional fast mode in the boundary layer continuously decreases from its initial high value up to the largest Reynolds number of 4000 computed in this study. For the slow mode it increases from its initial low value up to the Reynolds number of 4000, with a kink in between. For this frequency, Mack's first mode is unstable between Reynolds numbers of 580 to 1990 and the second mode is unstable between Reynolds numbers of 3020 to 3800 and the fast mode remains stable in this case. The figure also depicts the phase speed of the fast and slow acoustic waves for zero incidence angles. The perfect phase speed matching with the acoustic waves occurs at Re = 100 for the slow mode and *Re* = 200 for the fast mode. For the unit Reynolds number of $7.2*10^6$/m, *Re* = 200 is located at 5.6 mm from the leading edge of the plate while the neutral point for the first mode is located close to *x* = 47 mm. Therefore, strong generation of instability waves is expected in the leading-edge region where bluntness and non-parallel effects will also become important. Comparison of Figure 2 and 3 shows that the phase synchronization of the fast and slow modes occurs well into the second mode instability region, while the phase speed of the fast mode equals unity just ahead of the second mode neutral point.

3.3 Mean flow

Figure 4 shows the mean flow density contours extracted from the Navier-Stokes computations. Figure 4(a) shows the entire domain for the leading edge bluntness of *2b* = 0.0005 cm. and Figs. 4 (b), (c), (d) show the flow field near the leading edge for the leading edge bluntness *2b* = 0.0005, 0.005, 0.05 cm. The leading edge shocks are located approximately at 0.0003, 0.0007 and 0.0040 cm. upstream of the leading edge. Figure 5 shows the mean pressure distribution along the surface for the three different bluntness cases. The density profiles at *x* = 0.01, 0.05, 0.20, 0.50, 1.0 1.5 meters. ($\sqrt{\mathrm{Re}_x}$ = 268, 600, 1200, 1897, 2683, 3286) are plotted in Fig. 6(a) for the case 2b = 0.0005 cm. Figure 6(b) shows the same profiles in the similarity coordinates. The compressible Blasius similarity profile is also included for comparison. It is seen that very close to the leading edge, there exists a strong shock and that the associated compression is followed by an expansion over the leading edge and the shock becomes weaker away from the leading-edge region. The boundary layer profiles slowly approach the Blasius similarity profile close to *x* = 0.5 meters.

Figure 7(a) shows the comparison between the growth rate computed using the similarity profiles and the profiles obtained from the numerical simulation for the wave with $F = 0.6*10^{-4}$. Figures 7(b) and (c) show the second derivative of the temperature for the two mean profiles at the station *x* = 0.5 and 2.0 meters. It is seen that the stability results obtained using the Navier-Stokes mean flow for the two small bluntness cases agree reasonably well with those obtained using the Blasius similarity profiles. However, for *2b* = .05 cm, there is significant difference both for the mean flow and the stability results. Another

observation is the difference between the stability curves for the fast and the slow modes for the $2b = 0.05$ case. Though both modes are stable near the leading edge, the fast mode is less stable than the slow mode. This difference in damping rates of the modes may become a discriminator in determining the relative significance of the receptivity mechanisms associated with slow and fast acoustic waves in this case.

3.4 Interaction of slow and fast acoustic waves with the boundary layer

After the mean flow is computed, two-dimensional slow and fast acoustic waves are introduced at the outer computational boundary. The computations are performed for three frequencies F = 2.2, 1.1 and $0.6*10^{-4}$. For the unit Reynolds number of the computation, these correspond to 182.6 kHz, 91.3 kHz and 49.8 kHz, respectively. The amplitude of the acoustic waves forced at the outer boundary are $\tilde{p}_{ac}/p_{\infty} = 0.0001$ for the frequencies $F = 2.2*10^{-4}$ and $1.1*10^{-4}$ and $\tilde{p}_{ac}/p_{\infty} = 0.00001$ for the low frequency $F = 0.6*10^{-4}$. Since lower frequencies yield larger integrated amplification, the smaller forcing amplitude for the latter case keeps boundary layer disturbances in the linear regime. The highest frequency was selected to match that used in Ref. [12] while the intermediate frequency was .5 times the highest. The lowest frequency was selected to yield large disturbance growth. High frequency disturbances are introduced first in the boundary layer and grow to small amplitudes and then decay. Low frequency disturbances become unstable further downstream but grow to larger amplitudes and lead to boundary layer transition in low disturbance environments.

Figure 8 shows the results for the evolution of the unsteady fluctuations obtained from the simulation for the slow wave at a fixed time. Figure 8(a) shows the contours of the density fluctuations in the entire domain and Fig. 8(b) depicts the results inside the boundary layer. The perturbation field can be divided into four regions. One region is the area outside the shock where the acoustic waves propagate uniformly. The second region is the shock layer across which the acoustic waves are transmitted. The third region is the area between the shock and the boundary layer. This region consists of transmitted external acoustic field and the disturbances that are radiated from the boundary layer. The fourth region is the boundary layer where the boundary layer disturbances evolve. The figures show that the disturbances inside the boundary layer originate in the leading-edge region. The figure also illustrates the evolution of the first mode near the leading-edge and the transformation of the first mode to the second mode in the downstream.

Figure 9 shows the evolution of wall pressure fluctuations induced due to the slow and fast acoustic waves of three different frequencies. Note that in Fig. 9, different vertical scales are used to present results for the slow and fast modes. This is because the slow mode is much more efficient in generating boundary layer instability; the second mode amplitude for the $F = 0.6*10^{-4}$ case is about 20 times higher for the case of slow acoustic wave as compared to the case with fast acoustic wave. Fedorov [11] computed response to the fast and slow acoustic waves for a frequency of $0.5*10^{-4}$ and found that the response to the slow acoustic waves is almost 50 times that of the fast acoustic waves. Thus, the present results, based on direct Navier-Stokes simulations, are in qualitative agreement with the theoretical results of [11]. This ratio is about 15 for $F = 1.1*10^{-4}$, although the second mode is not filtered out in the case of fast wave excitation. For the higher frequency case of $F = 2.2*10^{-4}$ and forcing with fast acoustic wave, Mack's second mode is buried in the computed signal which appears to be dominated by mode F. Ma and Zhong [12] also computed this same case and filtered out the second mode. Using their amplitude for the second mode, our results indicate that slow acoustic wave yields second mode amplitude that is about 10 times as large. Therefore, relative significance of receptivity via slow acoustic waves as compared to fast acoustic waves decreases with increasing frequency. However, excitation with slow mode is always dominant for the present case of adiabatic wall boundary layer.

Figure 10 shows the amplitude of the pressure fluctuations along the wall for the frequency $F = 0.6*10^{-4}$ using the log scale. Figure 10 also includes the results from the parabolized stability equations (PSE)

computations obtained for the same mean boundary layer profiles. The figures clearly show the initial generation and the eventual exponential growth of the instability waves inside the boundary layer. The slow wave whose wavelength is close to the wavelength of the instability wave near the leading edge transforms into instability waves rather directly. The growth of the disturbances agrees very well with the PSE results a short distance downstream of leading edge. Tracing the PSE results backward to the neutral point, the initial amplitude of the instability waves at the neutral point can be estimated. From these values the receptivity coefficients defined by the initial amplitude of the pressure fluctuations at the wall, non-dimensionalized by the free-stream acoustic pressure, can be evaluated:

$$C_{recpt,p_{wall}} = \frac{(p_{wall})_n}{p_{ac}} \tag{14}$$

The computed receptivity coefficients associated with the slow and the fast acoustic waves are

$$C_{recpt,p_{wall},S} = 9.0$$
$$C_{recpt,p_{wall},F} = 0.45 \tag{15}$$

Thus, the receptivity coefficient for the slow mode is 20 times that of the fast mode for the forcing frequency of $F = 0.6*10^{-4}$. The receptivity coefficients for the frequencies $F = 1.1, 2.2*10^{-4}$ are computed to be about 4 and 2, respectively, for the slow mode.

Here, the use of PSE to compute the receptivity coefficient is somewhat arbitrary as it does not trace the modes well at low Reynolds numbers; the approach is particularly problematic for the fast mode. However, what is important is the relative significance of the slow and fast modes and that information is correctly captured. Thus, instead of stating that the receptivity coefficient for the slow mode is 20 times that of the fast mode (for $F = 0.6*10^{-4}$) we could equally state that the maximum (linear) amplitude attained due to slow acoustic wave forcing is 20 times that for the case of fast acoustic wave forcing.

Figure 11 shows the wavenumber variation along the streamwise direction calculated from the wall pressure fluctuations generated by the slow and the fast acoustic waves for the frequency $F = 0.6*10^{-4}$. This is achieved by first decomposing the fluctuations into harmonic components of the form

$$p(x,z,t) = \tilde{p}(x)e^{-i\omega t} + c.c \tag{16}$$

and, then evaluating wavenumber of the fluctuations from the expression

$$\alpha(x) = \left(\frac{1}{i\tilde{p}(x)}\frac{\partial\tilde{p}(x)}{\partial x}\right) = \alpha_r + i\alpha_i \tag{17}$$

Results are shown for both the slow and fast modes. The figure also includes the wavenumber distributions obtained from linear stability computations. Downstream of the leading-edge region $x >$ 0.02 m, the wavenumber distribution computed using Eq. (17) agrees very well with the linear stability theory results. The interesting part is how the slow acoustic wave with a higher wavenumber interacts and merges with the instability waves inside the boundary layer. The wavenumber near the nose region first decreases slowly up to $x \sim 0.01$ m., it then increases slowly for $x > 0.01$ m. and merges with the first mode disturbance around $x \sim 0.02$ meters. The two solutions continue to agree beyond this point. The fast stability mode is also excited very near the leading edge as is evident by the agreement between the linear stability and the numerical simulation results. At a location close to $x = 1$ m, the wavenumber jumps to the values correspond to the slow mode. We also plotted the variation of the phase speed for the fast mode computed using linear stability theory. The location where the phase speed equals the free stream velocity ($C_r = 1.0$) is also marked in the figure. At this location, the fast mode intersects with the $C_r = 1.0$ continuous spectrum and is signified by a jump in the imaginary part of the eigenvalue for the fast mode.

3.5 Effect of Bluntness

To investigate the effect of leading-edge thickness on the stability and the receptivity process, computations are performed for three different thicknesses *2b* = 0.0005, 0.005 and 0.05 cm. Figure 12 shows the evolution of wall pressure fluctuations induced by the slow acoustic wave for the frequency $F = 0.6*10^{-4}$. The maximum amplitudes for these three cases are 0.0292, 0.0133 and $1.0 * 10^{-6}$. For the two smaller thicknesses of 0.0005 and 0.005 cm, the evolution of disturbances is similar except that the boundary layer becomes less unstable with increasing bluntness. The ratio between the maximum amplitudes for the leading-edge thicknesses of 0.0005 and 0.005 is 2.2 from numerical simulation and is 2.0 from PSE prediction. Hence, it can be argued that the receptivity becomes weaker with increasing bluntness but only by a small amount of about 10%. The more interesting results are for the larger thickness case *2b* = 0.05 cm, for which the Reynolds number based on leading edge radius is 1800. As noted earlier, the first mode is very stable for this case. In addition, the second mode unstable region is narrower and the peak growth rate is lower than the other two cases for the same frequency. Comparing with the PSE results, it is clear that the disturbance evolution computed from Navier-Stokes simulation essentially follows a path that is expected for the first and second mode disturbances. Thus, the slow acoustic wave excites the stable first mode very near the leading-edge region and, since this disturbance is stable, it decays by about two orders of magnitude before it starts to grow again in the unstable second mode region. The receptivity coefficient based on the disturbance amplitude near the neutral point $x = 1.0$ is about 0.004. However, this low value is an artifact of the strongly damped first mode region. The disturbance amplitude in the leading-edge region is of the same order as for the cases with smaller leading-edge thickness. Thus the overall effect of bluntness make the supersonic flat plate boundary layer akin to low speed boundary layers where TS neutral point is preceded by a strongly attenuated region making leading-edge receptivity less significant as compared to localized receptivity near the neutral point. Therefore, it will be interesting to investigate whether inter-modal exchange induced by fast mode forcing could yield higher disturbance amplitudes near the second mode neutral point.

A calculation was performed for the case of *2b* = .05 cm with forcing by the fast acoustic waves and the results are presented in Fig. 13. By comparing the results with those in Fig. 12 (see also Fig. 7(a)), it can be seen that the disturbance induced by fast waves do not decay as much in the first mode region, giving rise to the second mode maximum amplitude of $2.5176*10^{-5}$, which is about 21 times higher than that in the case of slow wave forcing. However, it is still lower by almost three orders of magnitudes when compared to the case of *2b* = .0005m. It can be concluded that while bluntness stabilizes the boundary layer, it does influence relative significance of forcing by slow and fast modes. It seems that anything that stabilizes first mode disturbances will enhance the significance of the mechanism of inter-modal exchange which is induced by forcing via fast acoustic waves. This observation is consistent with the finding of Fedorov [11] that wall cooling could lend significance to the mechanism of inter-modal exchange as compared to forcing via the slow acoustic waves.

We note that the effect of bluntness on hypersonic boundary layer stability is much stronger for the flat-plate case as compared to circular cones (see [19]), due to much longer entropy swallowing distance in the former case. The strong stabilization of the boundary-layer due to small bluntness could be used to delay laminar-turbulent transition on hypersonic vehicles. In fact, this was earlier suggested by computations based on linear stability theory and the knowledge gained was used in the design of National Aero-Space Plane. The present direct numerical simulations have confirmed earlier findings based on linear stability theory.

3.6 Effect of Angle of Incidence

Computations are performed for three incident angles 10, 30 and 45 degrees. Figure 14 shows the unsteady density fluctuations and Fig. 15 shows the density fluctuations inside the boundary layer. Figure 15 shows the results at three different streamwise locations to illustrate the evolution of instability waves inside the boundary layer. First observation is that the acoustic waves are weakly transmitted through the shock in the lower part of the domain. This agrees with the prediction and analysis in Ref. [13], even though the leading edge was not properly resolved in their simulation. In the upper part, acoustic wave transmission through the shock is much stronger as evident from the disturbed flow field between the plate and the shock. Figure 16 shows the amplitude of the pressure fluctuations at the lower and upper side of the wall for the three incident angles. The maximum amplitudes at the upper (leeward) and the lower (windward) sides of the plate and their ratio are given in Table 4.

It is seen that the maximum amplitudes are smaller on the lower (windward) side compared to the upper (leeward) side. This effect increases with increasing angles of incidence. For incidence angles of 10, 30 and 45 degrees the ratio between the maximum amplitudes at the upper and the lower sides are 1.5, 2.2 and 2.5, respectively. Hence the receptivity becomes weaker on the lower side compared to the upper side with increasing incidence angles. The maximum amplitude increases by a small amount for 10 degrees incidence angle and then decreases slowly for larger incidence angles. For the 45 deg case, maximum disturbance amplitude in the boundary layer drops by a factor of about 1.7. For the windward side, the maximum disturbance amplitude drops at a faster rate; it decreases by a factor of 4.3 when incidence angle increases from 0 to 45 deg. Our finding that the response of the top boundary layer to the acoustic waves incident from below is stronger than that of the bottom boundary layer does not seem to support Kendall's [3] expectation "that waves arriving from the lower half of the tunnel do not affect the plate topside boundary layer".

Table 4 Maximum amplitudes of pressure fluctuations for different incident angles

θ_y	Lower	Upper	Ratio =Upper/Lower
0	0.0293	0.0293	1.0
10	0.0232	0.0330	1.5
30	0.0132	0.0290	2.2
45	0.00683	0.0169	2.5

Figure 17 shows wall pressure fluctuations on the log scale for the incidence angles of 10, 30 and 45 degrees. It is seen that near the leading edge, the upper side is disturbed more than the lower side. The initial amplitudes are essentially larger on the upper side as compared to the lower side and the ratio of the two, as given in the table, increases to 2.5 when the incidence angle is increased to 45 degrees.

Ma and Zhong [20] also studied the effect of incidence angle for the Mach 4.5 boundary layer and found that the response coefficient decreases with the incidence angle of the slow acoustic wave. We note that qualitatively similar results with respect to the effect of incidence angle were obtained in the study carried out by Egorov et al. [13], albeit at a higher Mach number. As pointed out earlier, leading edge was treated as an unresolved singularity in Ref [13] as well as in [20], while it was properly resolved by

providing a sufficient number of grid points in the present study. Therefore, we make the observation that the shape of the leading edge does not seem to have a profound effect on at least the qualitative characteristics of the receptivity process.

4 Conclusions

The response of a boundary layer to two-dimensional slow and fast acoustic waves is numerically investigated for a free stream Mach number of 4.5 and at a Reynolds number of $7.2*10^6$/meter. Both the steady and unsteady solutions are obtained by solving compressible Navier-Stokes equations using the 5^{th}-order accurate weighted essentially non-oscillatory (WENO) scheme for space discretization and using a third-order total-variation-diminishing (TVD) Runge-Kutta scheme for time integration. The geometry considered is that of a flat plate with a finite-thickness leading edge, which is resolved by providing a sufficiently dense grid in that region.

The results show that the instability waves are generated very close to the leading edge and the receptivity coefficient is about 9 times the amplitude of the forced slow acoustic wave. It is also found that the amplitude of the instability waves generated by the slow acoustic waves is about 20 times larger than that for the case of fast acoustic waves. Therefore, forcing by slow acoustic waves should result in earlier transition in supersonic and hypersonic boundary layers.

Computations are performed to study the effect of leading edge thickness and it is found that bluntness has a significantly stabilizing influence on the boundary layer, even for a relatively low Reynolds number based on the leading edge radius of 1800. It is also found that the role of fast acoustic waves is enhanced by bluntness as, in this case, the inter-modal exchange mechanism yields higher disturbance amplitude at the second mode neutral point location when compared to the case of forcing with slow acoustic waves. The stabilizing effect of small leading edge bluntness can be employed for transition delay in the design of hypersonic vehicles.

The effect of incidence angle of the acoustic waves is also studied and it is found that the receptivity of the boundary layer on the 'windward' side (with respect to the incident waves) decreases by a factor of 4.3 when the incidence angle is increased from 0 to 45 deg. On the other hand, receptivity of the boundary layer on the 'leeward' side varies relatively weakly with the incidence angle. In this case, maximum disturbance amplitude in the boundary layer first increases by a factor of 1.1 and then drops by a factor 1.7 when the incidence angle increases to 45 deg.

References

1. Goldstein, M. E., "The evolution of Tollmien-Schlichting waves near a leading-edge", J. Fluid Mechanics, Vol. 127, 1983, pp. 59-81.
2. Goldstein, M. E., "The generation of Tollmien-Schlichting waves by long wavelength free stream disturbances", *Stability of Time Dependent and Spatially Varying Flows*, ed. D. L. Dwoyer & M. Y. Hussaini, Springer Verlag, 1987, pp. 58-81.
3. Kendall, J. M., "Wind tunnel experiments relating to supersonic and hypersonic boundary layer transition", AIAA J., Vol. 13, 1975, pp. 290-299.
4. Fisher, D. F., and Dougherty, N. S., "In-Flight Transition Measurement on a 10 deg cone at Mach numbers from 0.5 to 2.0", NASA TP-1971, 1982.
5. Mack, L. M., "On the application of linear stability theory and the problem of supersonic boundary-layer transition", AIAA J., Vol. 13, 1975, pp. 423-448.

6. Gaponov, S. A., “Interaction between a supersonic boundary layer and acoustic disturbances,” *Fluid Dynamics*, 6, 1977.

7. Gaponov, S. A. and Smorodsky, B. V., “Supersonic Boundary Layer Receptivity to Streamwise Acoustic Field,” *IUTAM Symposium,*, Spinger-Verlag, 1999.

8. Mack, L. M., “Boundary layer stability theory”, Report 900-277 Rev. A, Jet Propulsion Lab, Pasadena, CA, 1969.

9. Fedorov, A. V., and Khokhlov, A. P., “Excitation of Unstable Modes in a Supersonic Boundary Layer by Acoustic Waves,” *Fluid Dynamics*, No. 9, pp. 456-467, 1991.

10. Fedorov, A. V., and Khokhlov, A. P., “Prehistory of Instability in a Hypersonic Boundary Layer”, Theoret. Comput. Fluid Dynamics, Vol. 14, 2001, pp. 359-375.

11. Fedorov, A. V., “Receptivity of a high-speed boundary layer to acoustic disturbances”, J. Fluid Mechanics, Vol. 491, pp. 101-129.

12. Ma, Y., and Zhong, X., “Receptivity of a Supersonic Boundary Layer over a Flat Plate. Part 2. Receptivity to free-stream sound”, J. Fluid Mechanics, Vol. 488, 2003, pp. 79-121.

13. Egorov, I. V., Fedorov, A. V., and Soudakov, V. G., “Direct numerical simulation of supersonic boundary-layer receptivity to acoustic disturbances,” *AIAA Paper* 2005-97, 2005.

14. Malik, M. R., “Hypersonic Flight Transition Data Analysis Using Parabolized Stability Equations with Chemistry Effects,” Journal of Spacecraft and Rockets, Vol. 40, No. 3, 2003, pp. 332-344.

15. Shu, Chi-Wang, “Essentially Non-Oscillatory and Weighted Essentially Non-Oscillatory Schemes for Hyperbolic Conservation Laws,” *NASA/CR-97-206253 and ICASE Report* N0. 97-6

16. Atkins, H. L., “High-Order ENO Methods for the Unsteady Compressible Navier-Stokes Equations,” *AIAA Paper 91-1557*, 1991.

17. Balakumar, P., Zhao, H., and Atkins, H., “Stability of Hypersonic Boundary Layers over a Compression Corner,” *AIAA Paper* 2002-2848, 2002.

18. Malik, M. R., “Numerical Methods for Hypersonic Boundary Layer Stability”, Journal of Computational Physics, Vol. 86, No. 2, 1990, pp. 376-413.

19. Malik, M. R., Spall, R. E. and Chang, C.-L., “Effect of Nose Bluntness on Boundary Layer Stability and Transition”, presented at AIAA 28th Aerospace Sciences Meeting, Reno, NV, January 8-11, 1990, AIAA Paper No. 90-0112.

20. Ma, Y., and Zhong, X., “Receptivity of a Supersonic Boundart Layer over a Flat Plate. Part 3. Effects of different types of free-stream disturbances”, J. Fluid Mechanics, Vol. 532, 2005, pp. 63-109.

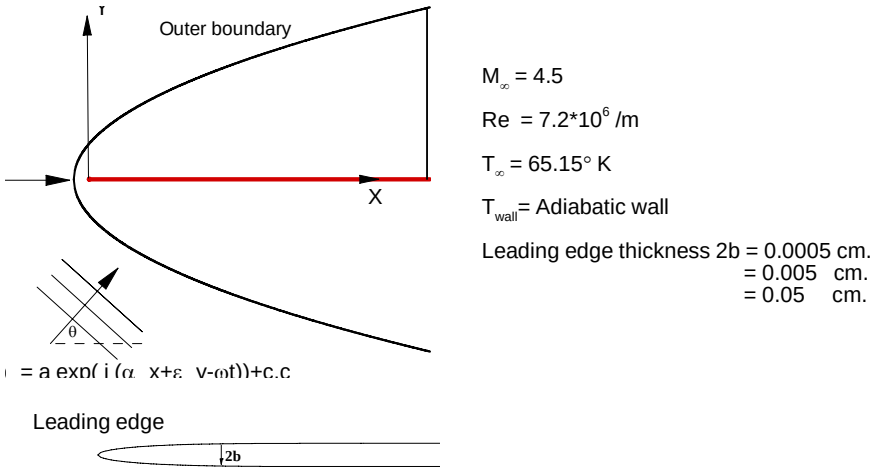

Figure 1. Schematic diagram of the computational model.

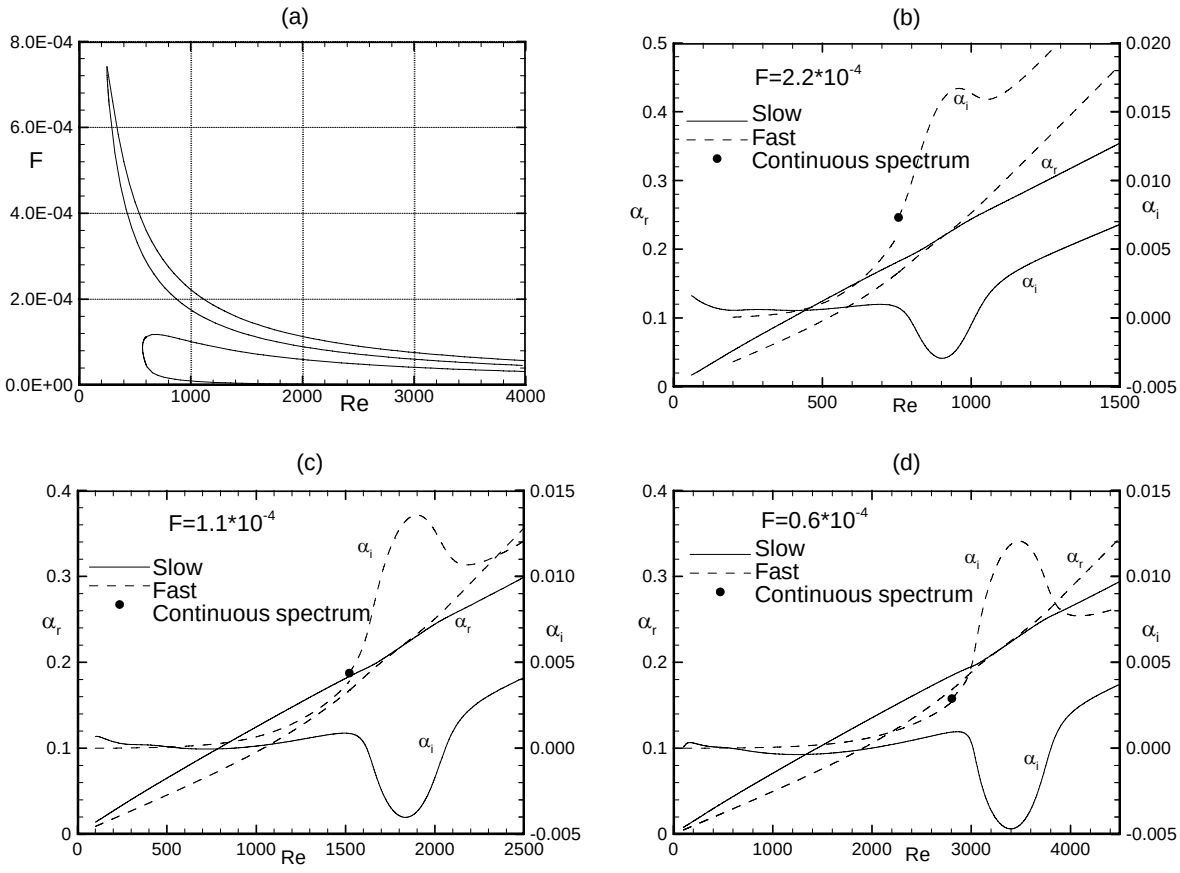

Figure 2. (a) Neutral stability diagram. (b), (c), (d) Eigenvalues (α_r, α_I) for fast and slow modes for F=2.2, 1.1, 0.6 *10^{-4}.The solid circle indicates the location where the fast mode intersects with the c_r=1.0 continuous spectrum.

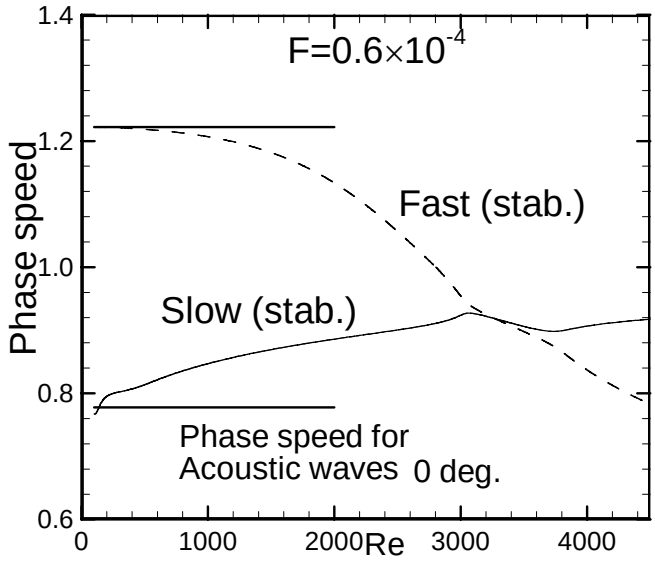

Figure 3. Variation of phase speed of the fast and slow instability modes along with the acoustic waves.

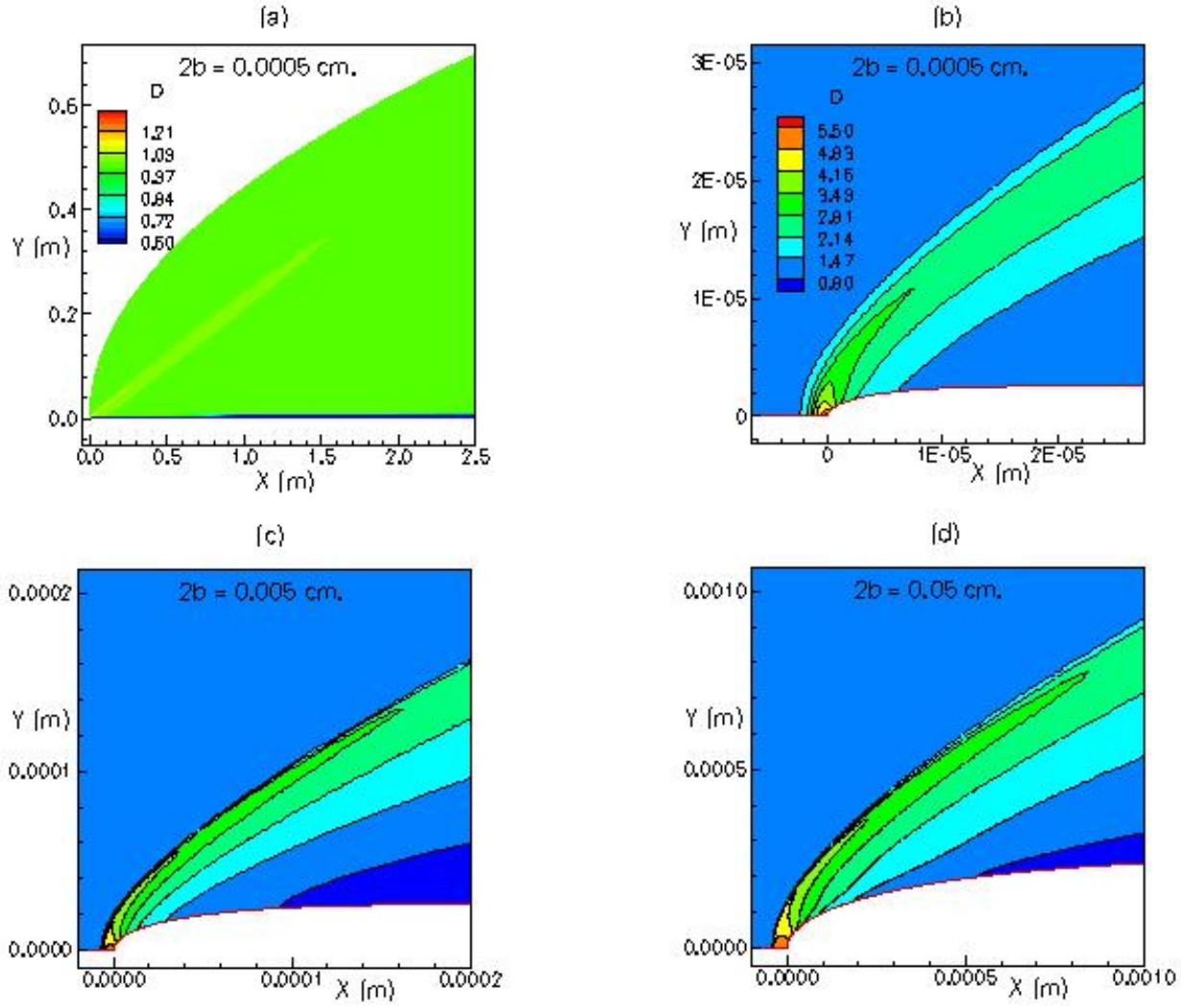

Figure 4. Computed density contours for Mach 4.5 flow over flat plates with leading-edge bluntness.

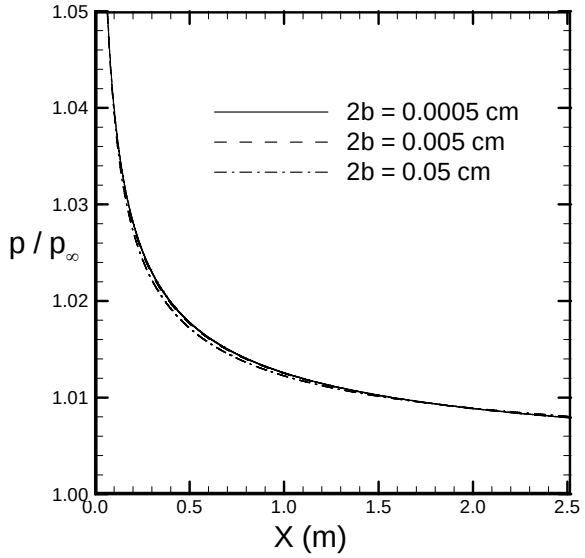

Figure 5. Pressure distribution along the surface for three levels of bluntness.

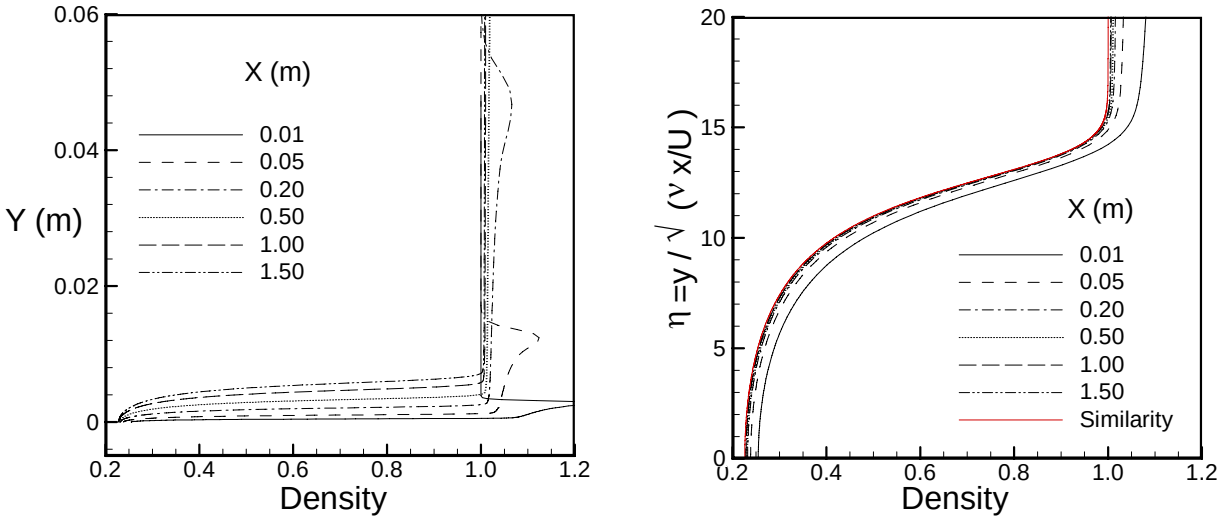

Figure 6. Mean density profiles at different X locations for 2b = 0.0005 cm.

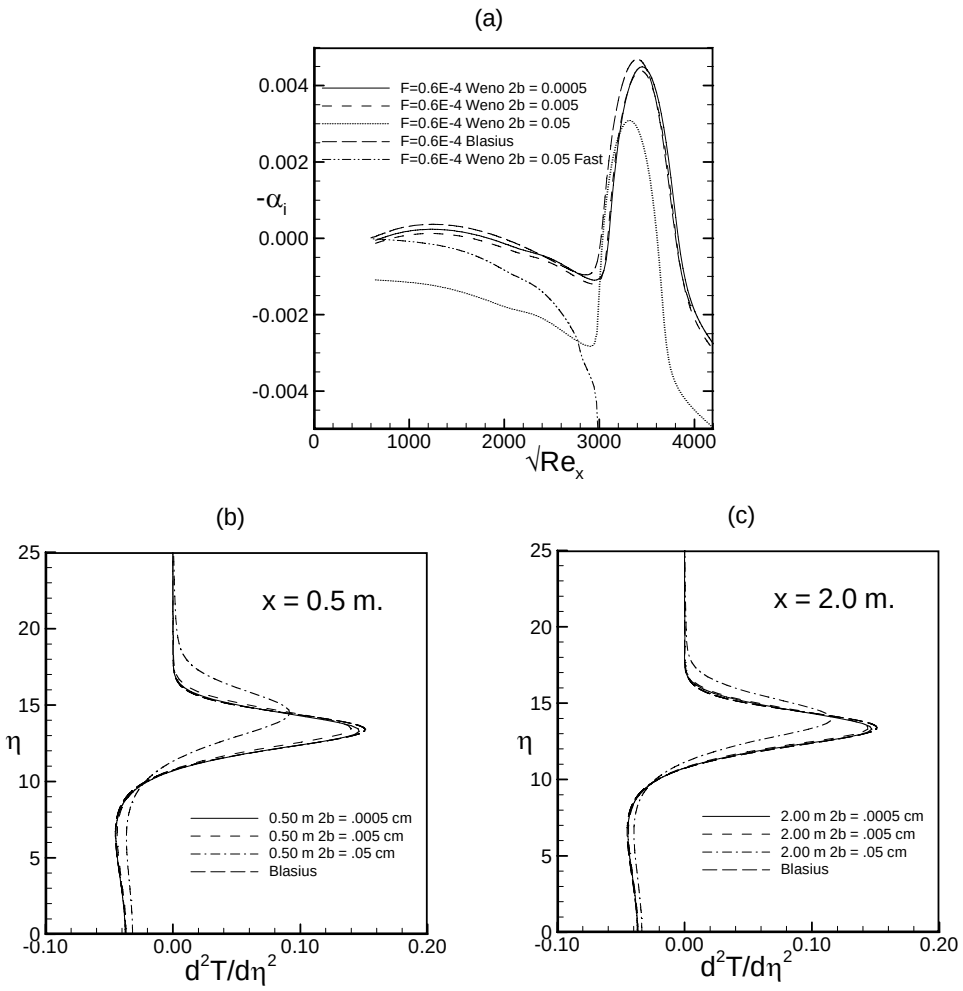

Figure 7. (a) Comparison of disturbance growth rate computed using the Blasius similarity profiles and the profiles from the numerical solution. (b), (c) Comparison of second derivatives for the temperature.

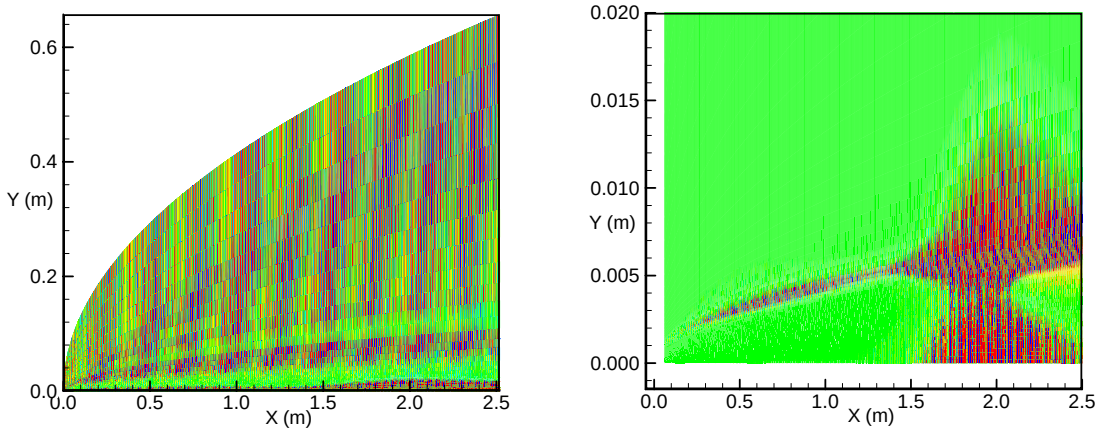

Figure 8. Contours of the unsteady density fluctuations due to the interaction of slow acoustic wave with a blunted flat plate: $F = 0.6*10^{-4}$, incident angle 0.0.

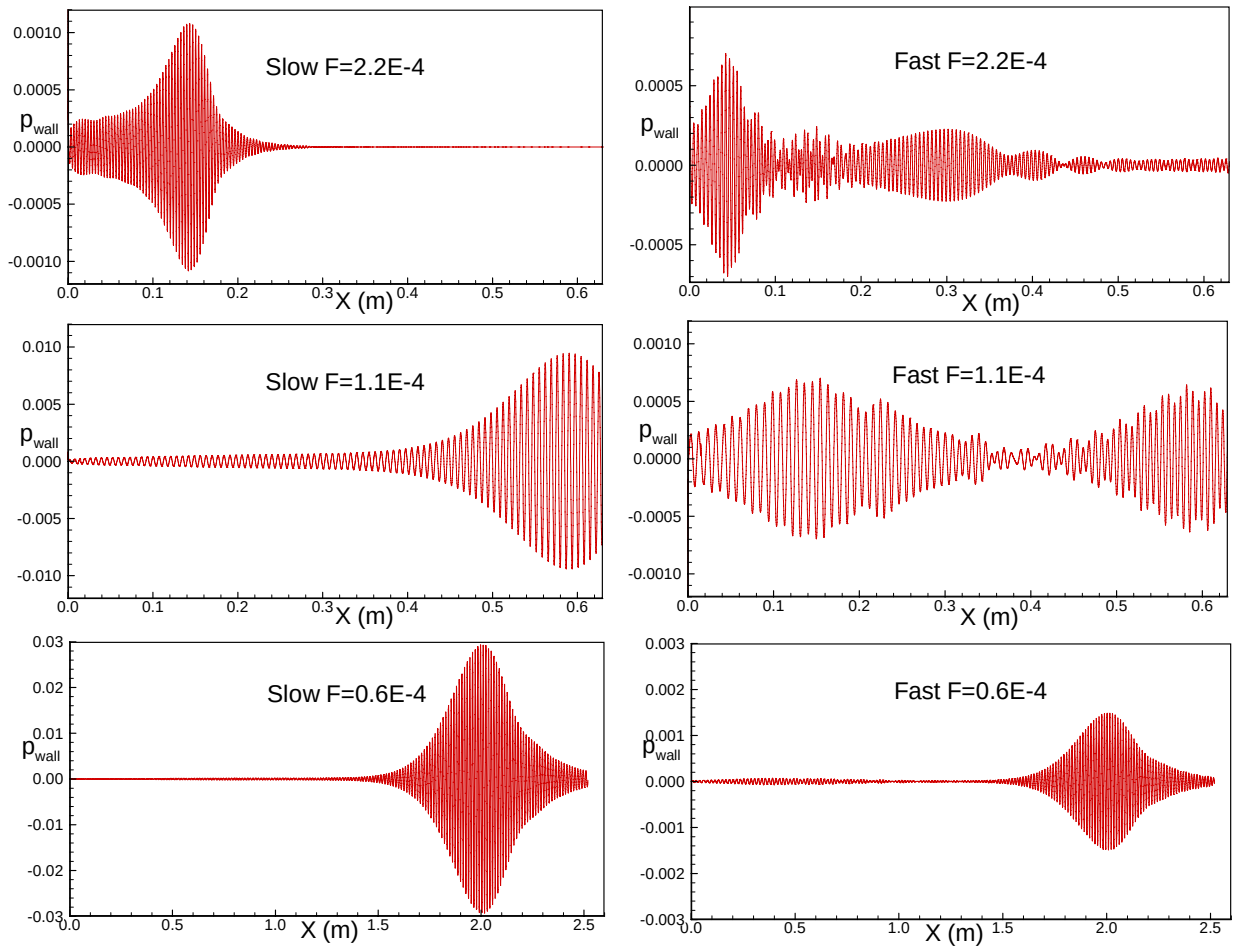

Figure 9. Wall pressure fluctuations generated by two-dimensional slow and fast acoustic modes for F=2.2, 1.1, 0.6*10^{-4}. (Note difference in scales)

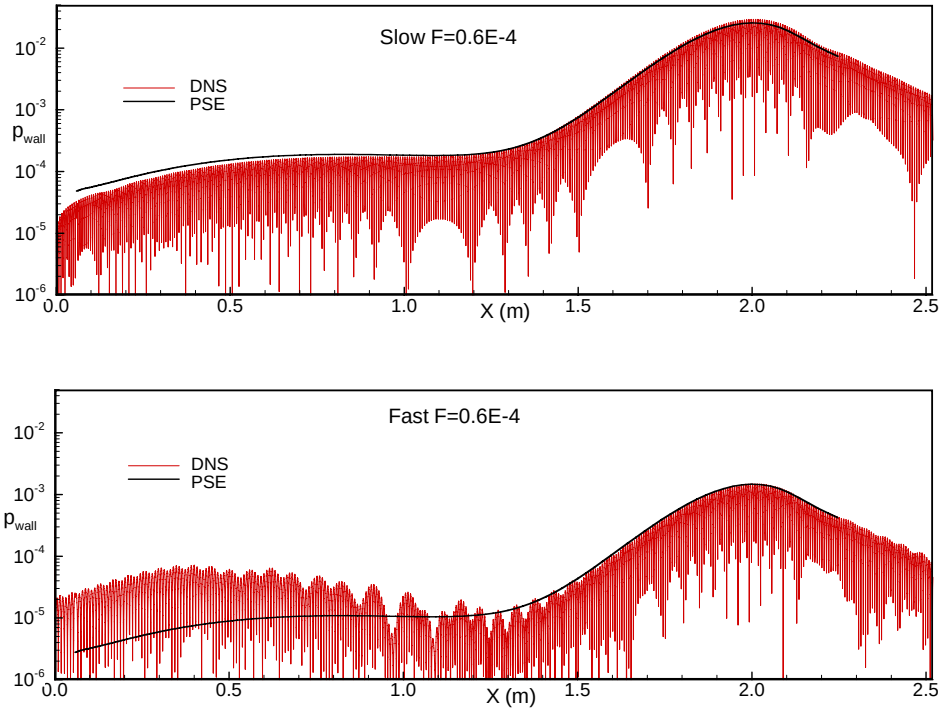

Figure 10. Amplitude of the pressure fluctuation at the wall and comparison with PSE results. F=0.6*10^{-4}, incident angle 0.0.

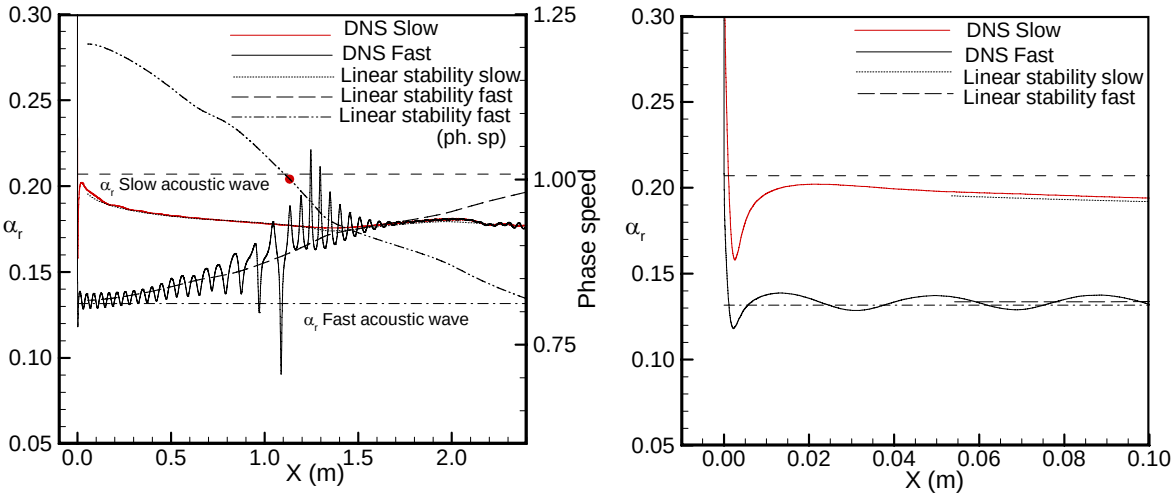

Figure 11. Wavenumber of the (wall) pressure fluctuation and comparison with linear stability results. F=0.6*10^{-4}, 2b = 0.0005.

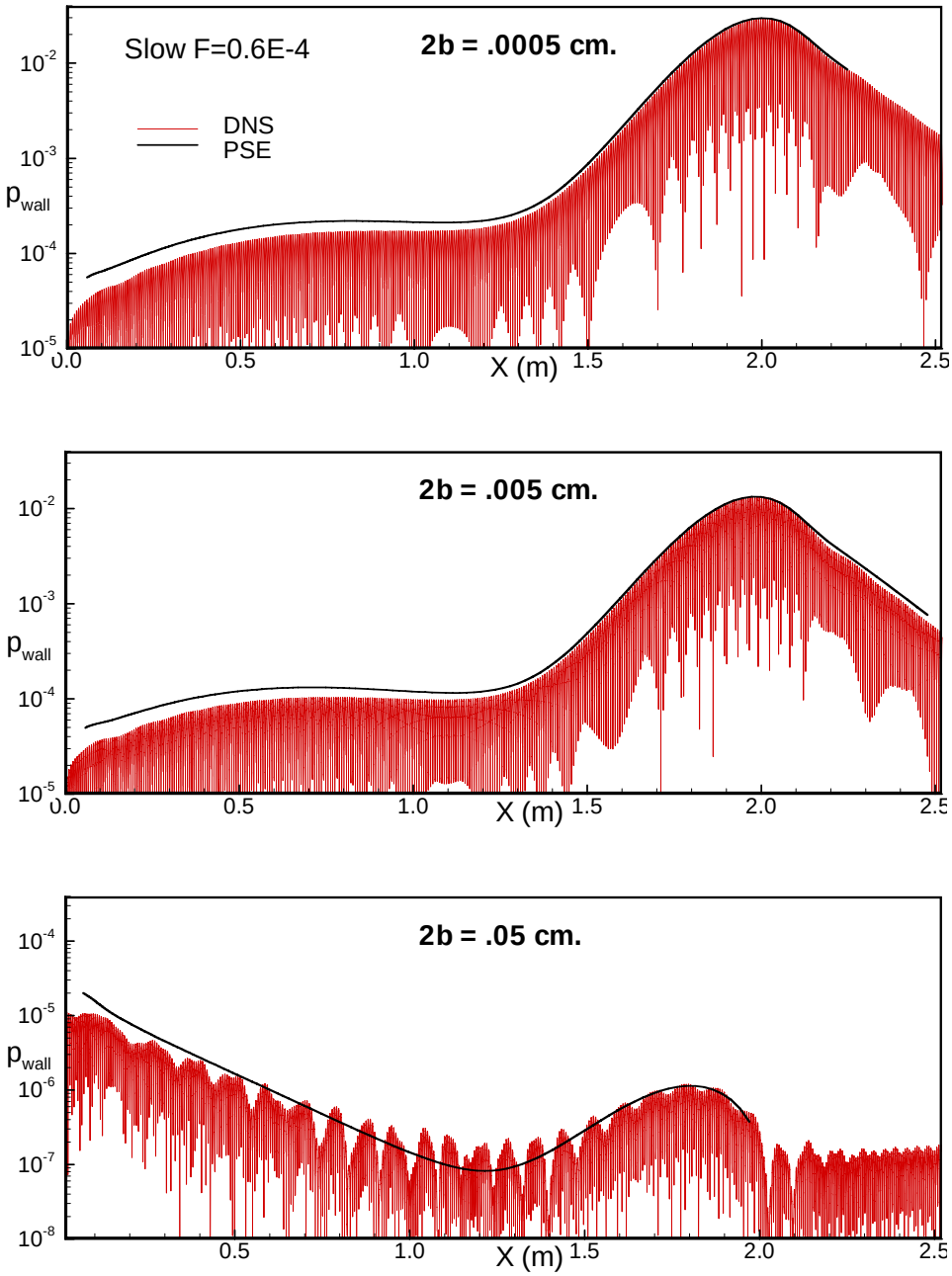

Figure 12. Wall pressure fluctuations generated by two-dimensional slow acoustic waves of for the flat-plate with thickness 2b and forcing frequency $F = 0.6*10^{-4}$.

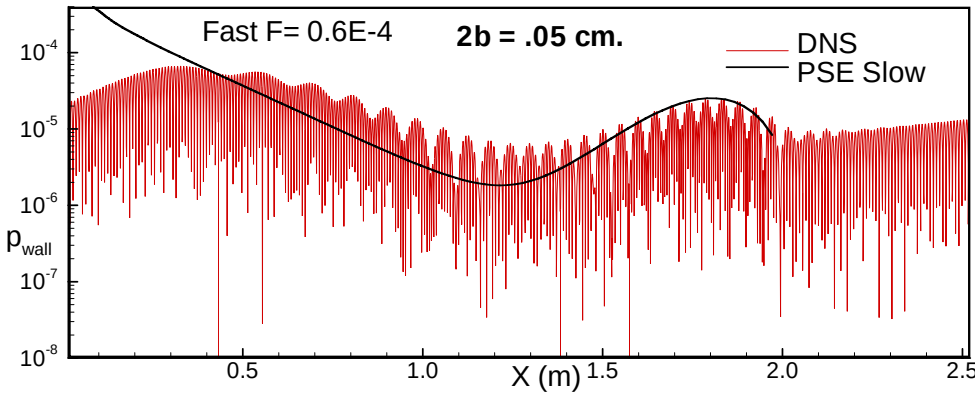

Figure 13. Wall pressure fluctuations generated by two-dimensional fast acoustic waves of frequency F = 0.6*10^{-4}.

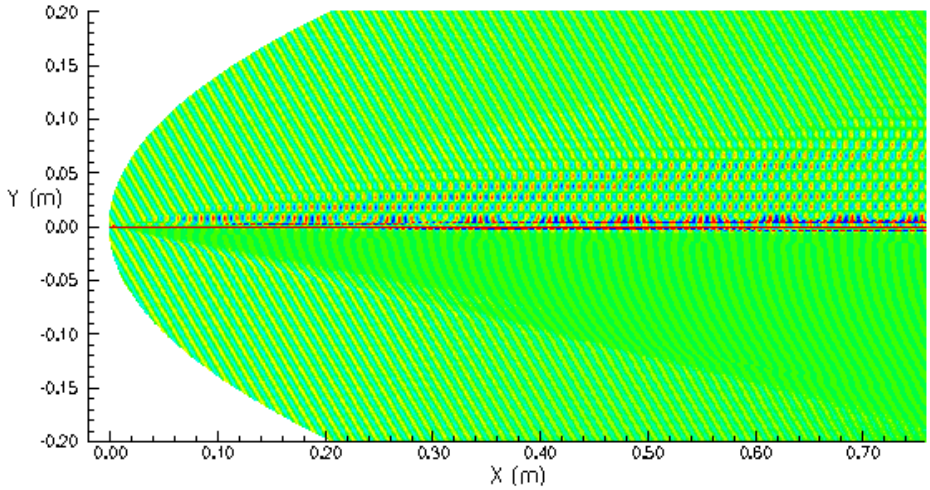

Figure 14. Contours of the unsteady density fluctuations due to the interaction of slow acoustic wave of frequency F = 0.6*10^{-4} (incident from below at an angle of 30 deg) with a flat plate with thickness 2b = 0.0005 cm.

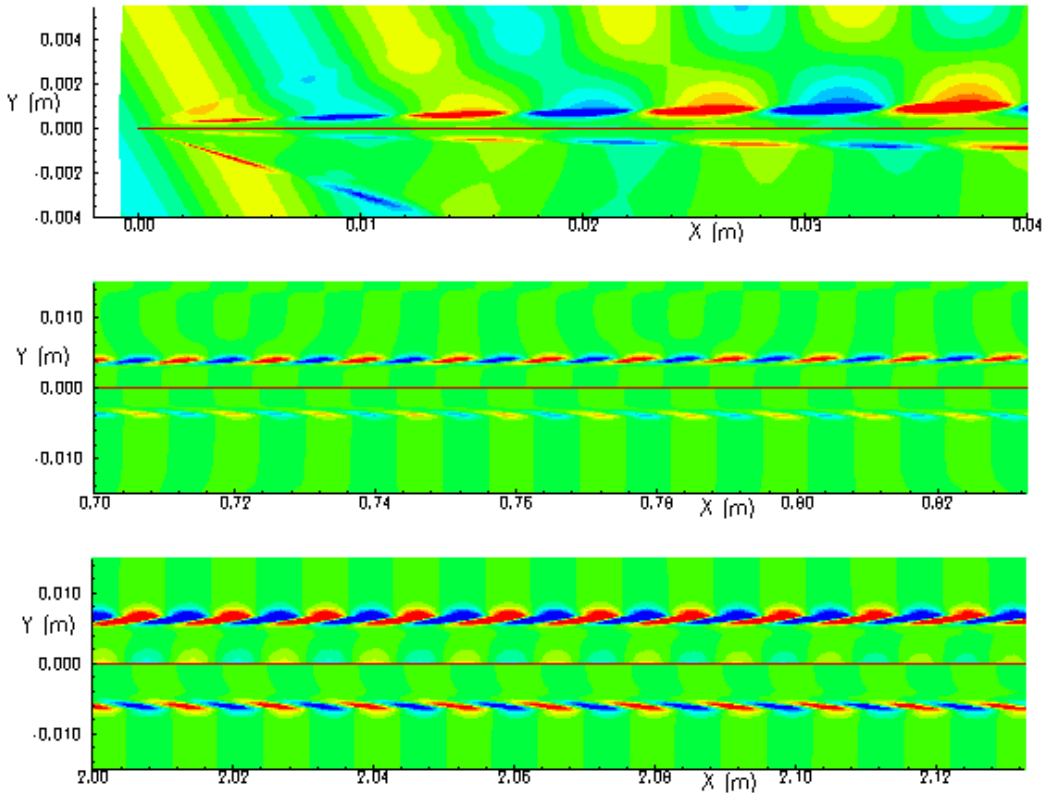

Figure 15. Results of Figure 14 on an expanded scale to show details.

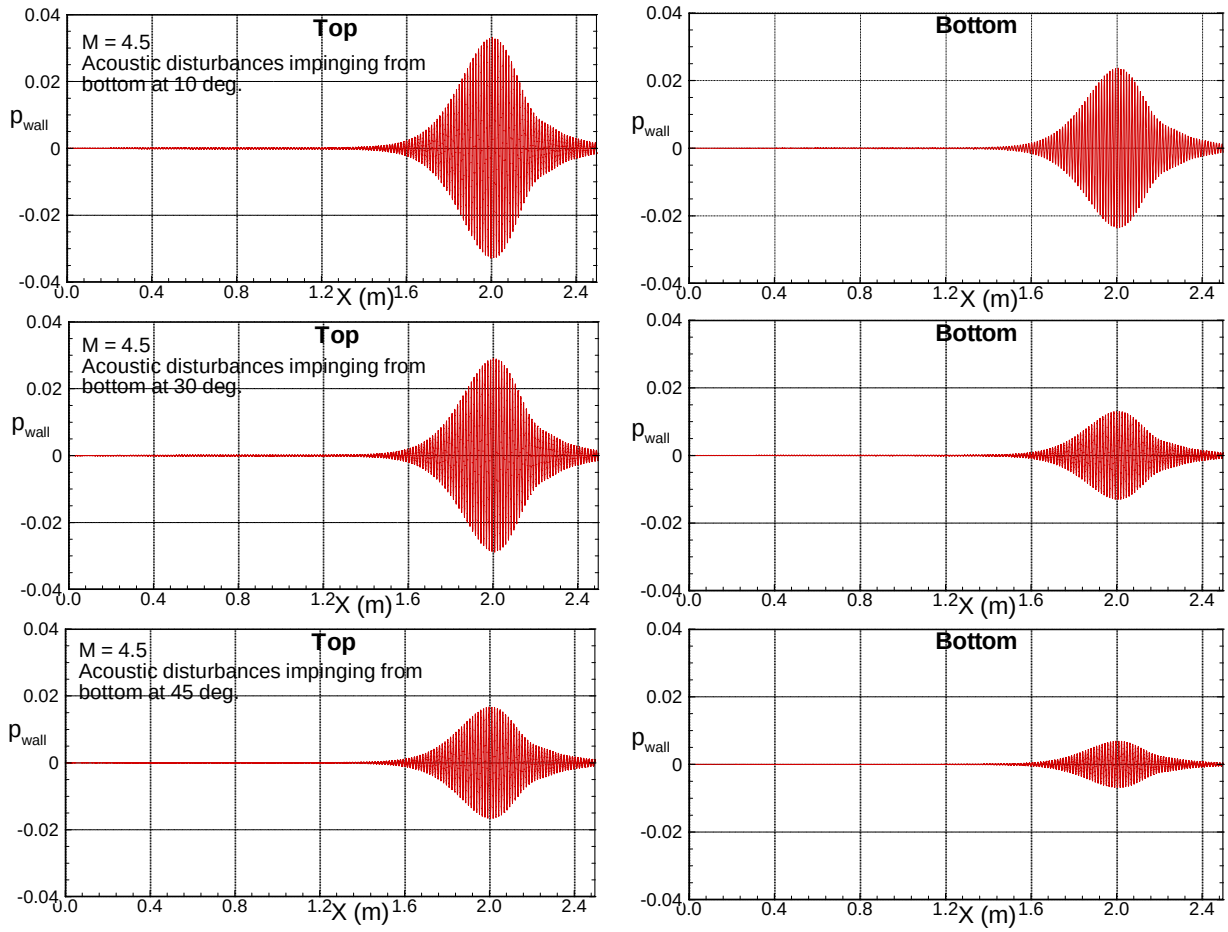

Figure 16. Pressure fluctuations on the top and bottom surfaces of the flat-plate (2b=.0005) generated by two-dimensional slow acoustic wave of frequency $F = 0.6*10^{-4}$, incident from below at different angles.

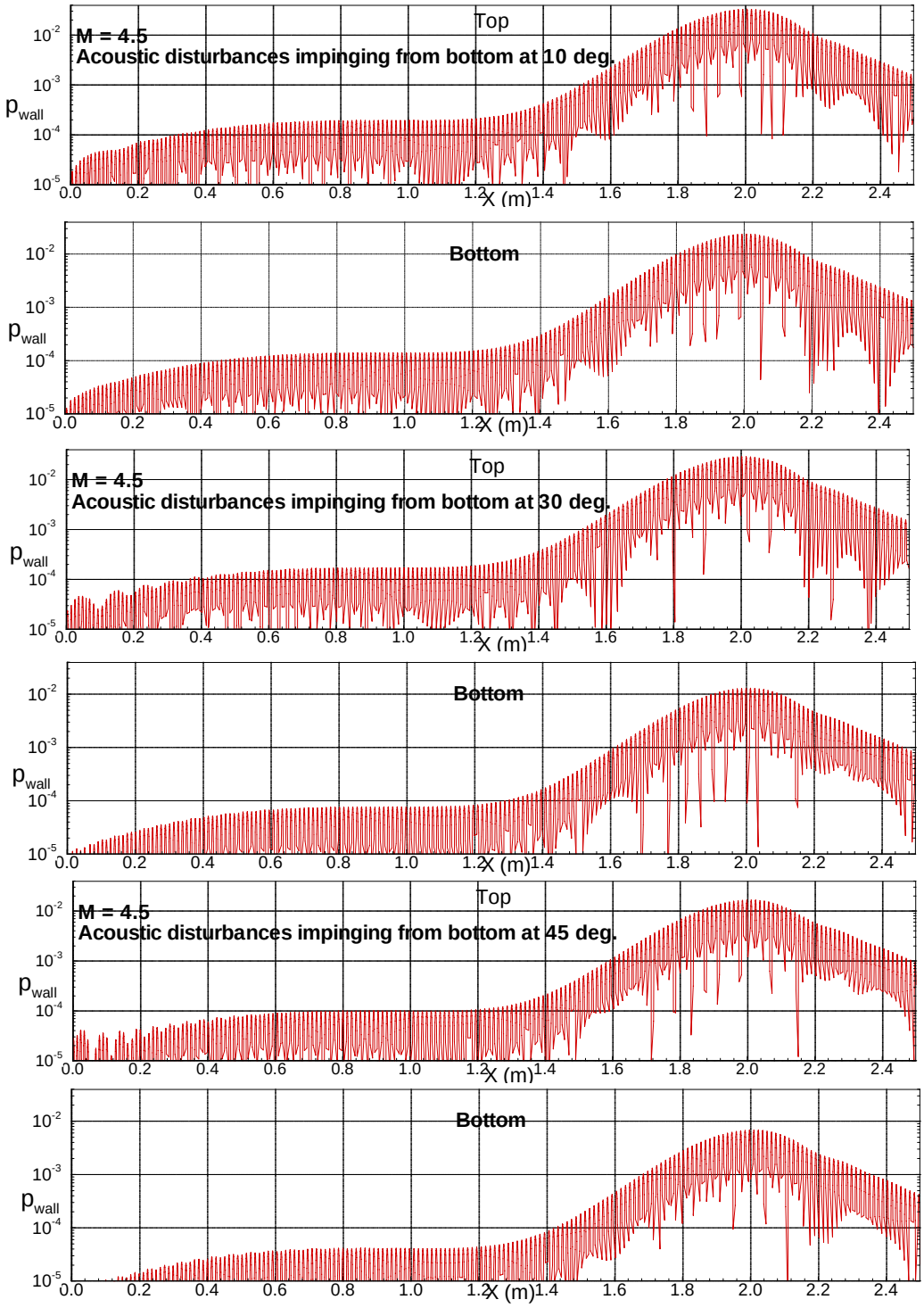

Figure 17. Results of Figure 16 plotted on the log-scale.